PLEASE SCROLL DOWN FOR TEXT.

Spiking Behaviour in Laterally-Coupled Pairs of VCSELs With Applications in Neuromorphic Photonics

Matěj Hejda ⬤, Martin Vaughan ⬤, Ian Henning ⬤, Rihab Al-Seyab ⬤, *Member, IEEE*, Antonio Hurtado ⬤, and Mike Adams ⬤

Abstract—We report a theoretical study on laterally-coupled pairs of vertical-cavity surface-emitting lasers (VCSELs) operated under conditions that generate or suppress high-speed optical spiking regimes, and show their potential in exemplar functionalities for use in photonic neuromorphic computing systems. The VCSEL numerical analysis is based on a system of five coupled mode equations, which, for the case of weak coupling, are reduced to a set of three equations that predict the saddle-node stability boundary in terms of device parameters and operating conditions. These results guide numerical simulation to demonstrate multiple neuron-like dynamics, including single- and multiple-spike emission, spiking inhibition, and rebound spiking directly in the optical domain. Importantly, these behaviours are obtained at sub-nanosecond rates, hence multiple orders of magnitude faster than the millisecond timescales of biological neurons. The mechanisms responsible are explained by reference to appropriate phase portraits. The coupled VCSELs model is then used for demonstration of high-speed, all-optical digital-to-spiking encoding and for representation of digital image data using rate-coded spike trains.

Index Terms—VCSEL, laterally-coupled lasers, neuromorphic photonics, spiking laser neuron.

I. INTRODUCTION

RESEARCH into the use of light-powered systems for signal processing is an area of considerable and growing interest. Simultaneously, the availability of efficient artificial intelligence (AI) optimized hardware becomes more and more important as AI approaches grow in significance and complexity.

Matěj Hejda and Antonio Hurtado are with the Institute of Photonics, SUPA Department of Physics, University of Strathclyde, Glasgow G1 1RD, U.K. (e-mail: matej.hejda@strath.ac.uk; antonio.hurtado@strath.ac.uk).

Martin Vaughan, Ian Henning, and Mike Adams are with the School of Computer Science and Electronic Engineering, University of Essex, Colchester CO4 3SQ, U.K. (e-mail: martin.vaughan@physics.org; idhenn@essex.ac.uk; adamm@essex.ac.uk).

Rihab Al-Seyab is with the School of Computing and Engineering, University of Gloucestershire, Cheltenham GL50 2RH, U.K. (e-mail: ralseyab@glos.ac.uk).

Among the novel, AI-focused hardware architectures, neuromorphic (brain-inspired) computing based upon photonic technologies has emerged notably over recent years, demonstrating implementations of photonic spiking neural networks (pSNNs) and photonic spike processing systems. These aim to exploit the fast neuron-like spiking dynamical behaviour occurring in different optical elements, such as semiconductor lasers (SLs), as part of novel computational approaches. High-speed optical spiking dynamics have been demonstrated both numerically and experimentally in various SL systems [1], [2] including quantum dot lasers [3], integrated DFB lasers [4], [5], two-section lasers with saturable absorber (SA) [6], semiconductor ring lasers [7], photonic crystals [8], [9], fiber lasers with graphene SA [10], lasers coupled to resonant tunnelling diodes [11], [12] and vertical cavity surface emitting lasers (VCSELs) both in single section and two-section layouts.

Thanks to their mature and scalable technology, VCSELs operating as all-optical spiking devices are gathering increasing research interest [13]. In single-section devices, excitation and inhibition of sub-nanosecond spiking dynamics was demonstrated via amplitude [14], phase [15] and electrical [16] modulation, with character of spiking responses depending on stimuli type [17]. Practical computational tasks have been experimentally demonstrated in injection-locked VCSELs, including photonic processing [18] and temporal domain encoding [19] of images. Propagation of generated spiking events between in-series connected VCSEL-neurons has also been experimentally demonstrated [20], paving the way towards interconnected architectures of multiple VCSEL-based photonic spike processing platforms. Furthermore, two-section VCSEL-SAs have been demonstrated as analogous to leaky integrate-and-fire (LIF) class neurons [21] and utilized in coupled arrangements for spike synchronization [22], pattern recognition [23], winner-takes-all algorithms [24], spike sequence learning [25] and motion detection [26].

This work provides a first exploration of the use of laterally-coupled VCSELs in order to generate, inhibit and apply controllable optical spiking patterns for use in on-chip photonic neuromorphic computing platforms. Laterally-coupled VCSELs are formed by designing a structure such that there is overlap of the lateral optical fields between two adjacent VCSELs. Previously, laterally coupled VCSELs with integrated passive cavities have shown promise for enhancing modulation bandwidth, an

approach which has been reported for single VCSEL-passive cavity devices [27], [28], [29] as well as multiple coupled cavities in two-dimensional hexagonal 'superstructure' [30]. In this work, we assume an array of homogeneous, laterally coupled VCSELs (active devices) forming a set of coupled oscillators, with spiking in mixed active-active and active-passive coupled elements representing an interesting future research direction.

The strength of the coupling between VCSELs is determined by the magnitude of overlap of the fields and can be calculated using coupled mode theory [31]. Examples of practical realisations of laterally-coupled VCSELs include proton implantation technology to provide both electrical isolation and optical guidance [32] or ion implantation for current confinement and a photonic crystal etch for optical confinement [33]. The use of laterally-coupled devices offers the exciting potential of forming large integrated arrays of VCSEL-based artificial photonic neurons with overall reduced footprint, as well as permitting programmability to define areas of uniform or diverse functionality directly on-chip. In general, computational performance and ability to process more complex data in neural networks grows with the number of neurons, neuronal layers and synaptic links. Hence, for the development of future spike-based neuromorphic hardware with photonic artificial neurons, it is highly desirable that these have reduced spatial footprint and allow for on-chip integration. This will in turn allow for low-footprint, high-density layouts of pSNNs [34] to compete in performance with current CMOS-based neuromorphic platforms. Therefore, validation of spike-based processing tasks in the evanescently-coupled model significantly increases prospects of spiking VCSELs for delivering practical, chip-scale, photonics-powered neuromorphic systems.

This paper is organised as follows: Section II provides a discussion of the underlying coupled laser theory on which the work is based. Section III then describes via simulation how the coupled-lasers exhibit a range of neuron-like spiking behaviours along with some discussion of their origin. In Section IV we demonstrate the efficacy of this approach by using a selection of the behaviours in exemplar spike information encoding and processing scenarios, including digital-to-spiking format conversion and spike firing rate-coding functionality for digital image encoding. Finally, we conclude the work in Section V with a discussion of how the results of this work might be tested in experimental investigations.

II. THEORY

Theoretical modelling of spiking VCSEL neurons based on unidirectional optical injection has been based on the spin flip model (SFM) [20], [35], [36], [37], [38]. In this system, excitability is found within the injection-locking region of operation but only over small ranges ('homoclinic teeth') close to the saddle-node bifurcation [35]. This remains true for optically-injected lasers in the absence of polarisation effects where the SFM is not required to explain the fundamental behaviour [39]. Building on this it is therefore of interest to ask if behaviours, similar to those seen in master-slave configurations, can be found for laterally (mutually) coupled VCSELs. To investigate this

question, we use the normalised coupled mode equations which are known to provide a reliable description of two laterally-coupled lasers (denoted A,B here). These can be readily solved using numerical techniques [40]. In terms of normalised variables Y_A, Y_B for the field amplitudes, M_A, M_B for the carrier densities and ϕ as the phase difference between the fields in B and A, these equations can be written as:

$$\frac{dY_A}{dt} = \frac{1}{2\tau_p}(M_A - 1)Y_A - |\eta_{AB}|Y_B \sin(\theta + \phi) \quad (1)$$

$$\frac{dY_B}{dt} = \frac{1}{2\tau_p}(M_B - 1)Y_B - |\eta_{BA}|Y_A \sin(\theta - \phi) \quad (2)$$

$$\frac{d\phi}{dt} = \frac{\alpha_H}{2\tau_p}(M_A - M_B) - \Delta\Omega$$

$$+ \left[|\eta_{BA}|\frac{Y_A}{Y_B}\cos(\theta - \phi) - |\eta_{AB}|\frac{Y_B}{Y_A}\cos(\theta + \phi) \right] \quad (3)$$

$$\frac{dM_{A,B}}{dt} = \frac{1}{\tau_N}\left[Q_{A,B} - M_{A,B}(1 + Y_{A,B}^2) \right] \quad (4)$$

Equations (1)–(4) are rate equations derived from coupled mode theory allowing for a complex coupling rate [31]. Equations (1) and (2) describe the time evolution of the optical field amplitudes in VCSELs A and B. First RHS term of each of these equations gives the amplification of the field amplitude due to optical gain, and the second term accounts for coupling to the field in the other VCSEL. Equation 3 describes the time evolution of the phase difference between the fields in VCSELs A and B. The first term on the RHS gives the phase shift due to carrier effects, and the term in square brackets accounts for the phase change due to coupling. Equation 4 is the rate equation for the normalised carrier density in each VCSEL. The first term on the RHS describes the pumping and the second term accounts for radiative and non-radiative recombination as well as stimulated emission into the VCSEL mode (proportional to the mode intensity). Note that the factor of $\frac{1}{2}$ in the first terms on the RHS of (1)–(3) occurs since these describe field amplitudes whereas the optical gain here is that experienced by the field intensity. Within the Eqs, $\Delta\Omega$ is the angular frequency detuning between the cavity resonances of VCSELs B and A, α_H is the linewidth enhancement factor, τ_N is the carrier lifetime, τ_p is the photon lifetime and Q_A, Q_B are the normalised pumping rates. Allowance for asymmetric complex coupling has been made since the amplitudes $|\eta_{AB}|$, $|\eta_{BA}|$ of the coupling rates may differ, but the phase θ is assumed the same, since it has been shown for ring lasers that an asymmetry in phase has no influence on the topology of the phase space structure [41].

As mentioned above, the coupling rate is determined by lateral optical fields overlap of VCSELs A and B. This can be controlled by appropriate choice of the VCSEL parameters during fabrication. The strongest control parameter is the spatial separation of the VCSELs. For example, using a simple slab waveguide model for the VCSEL confinement, it has been shown [31] that the coupling rate amplitude varies exponentially and the coupling phase varies linearly with separation. Fundamentally, the real part of the coupling is determined by the real index guidance of

the VCSEL structures, whereas the imaginary part is governed by the gain difference. An experimentally estimated value for the weak coupling rate of a photonic crystal VCSEL array has been given as 30×10^9 rad/s [42]. For the same type of array, the imaginary part of the coupling rate has been experimentally estimated to vary from 150 GHz (moderate coupling) to 5 GHz (weak coupling) with increased pumping above threshold [43]. The coupling phase is found in the usual way from the ratio of imaginary and real parts of the complex coupling rate.

Given the wide range of parameters for this two-laser system, it is helpful to seek analytic approximations to identify promising operational conditions for numerical solutions. For the particular case of symmetric weak coupling ($|\eta_{AB}| = |\eta_{BA}| \equiv |\eta|$ with $|\eta|\tau_p \ll 1$) and equal pumping ($Q_A = Q_B$), approximate steady-state solutions of (1)–(4) as well as analytic expressions for the boundaries of regions of stability have been presented [31]. This work has been extended to account for unequal pumping by developing a 3-variable reduction of the coupled mode equations for real symmetric weak coupling, which yields approximate closed-form steady-state solutions and expressions for the stability boundaries [44]. The explicit result for the saddle-node (SN) bifurcation in [44] can be modified to apply to complex coupling rates, when it becomes:

$$|\Delta\Omega| < 2|\eta|\sqrt{\frac{1 + \alpha_H^2}{1 - q^2}}\sqrt{\sin^2(u + \theta) + q^2 \cos^2(u + \theta)} \quad (5)$$

where $u = \arctan(\alpha_H)$ and

$$q = \frac{Q_A - Q_B}{Q_A + Q_B - 2} \quad (6)$$

In the limit where $|\eta_{AB}| = 0$, (1)–(4) above describe the situation of an optically-injected laser with A as the master, B as the slave with an optical isolator between them. Thus (1) and the corresponding equation for laser A in (4) are no longer of interest and laser B is now described by only 3 equations. We find that if the phase θ of the coupling is taken as $-\pi/2$, then this analysis in the limit of small τ_p/τ_N yields the conventional result for the SN bifurcation in an optically-injected laser (see, e.g. [45]). In the present notation this takes the form:

$$|\Delta\Omega| < |\eta_{BA}|\frac{Y_A}{Y_{Bs}}\sqrt{1 + \alpha_H^2} \quad (7)$$

where Y_{Bs} is the steady-state value of Y_B in the presence of an optically-injected field of amplitude Y_A.

More generally, in the absence of an optical isolator but with the assumption of phase $\theta = -\pi/2$, the result (5) simplifies to:

$$|\Delta\Omega| < 2|\eta|\sqrt{\frac{1 + \alpha_H^2 q^2}{1 - q^2}} \quad (8)$$

It should be noted that the same result (8) is also obtained for phase $\theta = \pi/2$; in both cases, the coupling rate becomes purely imaginary. The influence of this $\pi/2$ phase shift in determining the dynamics of weakly-coupled lasers has been highlighted by Erzgräber et al. in an earlier study [40].
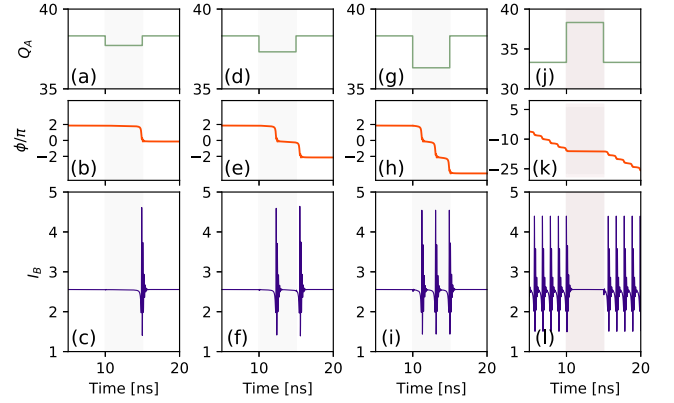

Fig. 1. Demonstration of activation and inhibition of spiking regimes in laterally coupled VCSELs. First row: Time traces of normalized pumping rate Q_A with modulation pulses of depth (a) -0.6, (d) -1.0, (g) -2.0 and (j) inhibitory pulse $+5.0$. Second row: phase difference between lasers B and A for Q_A pulses. Last row: intensity of laser B (I_B) showing activation of (c) single or (f,i) multiple spiking events as well as (l) inhibition of continuous spiking. All other parameter values are provided in the text.

III. NUMERICAL SIMULATION

A. Generation and Inhibition of Spiking

The rate equations (1)–(4) are solved numerically using a fourth-order Runga-Kutta method. For each set of solutions, the system was 'turned on' at time zero using a set of promising test conditions guided by theory, and the simulation was allowed to run to reach a steady state (typically 50 ns). Once steady state was reached, a modulation sequence was then applied to produce the test output for analysis. The simulations were run in MATLAB and both fixed and adaptive time step routines were compared to check for consistency in behaviour.

In this section, we focus on demonstrating fast controllable spiking regimes in laterally-coupled VCSELs. Fig. 1 shows how a fast spiking behaviour is triggered or inhibited by a 5 ns pulse of variable depth and polarity (negative pulse for excitation, positive for inhibiton) applied to the pump current of VCSEL A (Q_A). Here, we consider the situation where VCSEL A is pumped at a much higher rate, with weak symmetric complex coupling between the lasers ($|\eta_{AB}| = |\eta_{BA}| \equiv |\eta| = 2$) ns^{-1} with $\tau_p = 1.53$ ps, so that $|\eta|\tau_p = 0.00306 \ll 1$ and phase, $\theta = -\pi/2$. The carrier lifetime is $\tau_N = 1$ ns and the linewidth factor $\alpha_H = 2$. The first three columns in Fig. 1 utilize $Q_A = 38.32$, $Q_B = 3.48$ and the detuning between VCSELs B and A is taken as 2.6 GHz ($\Delta\Omega = 16.34$ rd/ns). For these Q_A, Q_B parameters, the value of q is 0.875, so that (8) gives the SN at $\Delta\Omega/2\pi = 2.66$ GHz, hence stable operation is expected for the detuning of 2.6 GHz assumed here. In Figs. 1(a), (d), and (g) the Q_A pulse depth is -0.6, -1.0, -2.0 respectively, and the corresponding q-values are then 0.873, 0.872 and 0.869 with SN boundaries shifted to 2.63 GHz, 2.62 GHz and 2.58 GHz, respectively. Figs. 1(c), (f), and (i) show the achievement of one, two or three spikes, respectively, in the output optical intensity of VCSEL B (I_B). A spiking event is accompanied by jumps of 2π in the phase difference ϕ for each spike between regions of stable
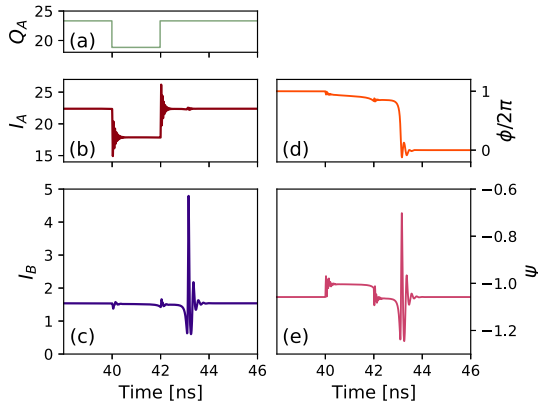
Fig. 2.   Time traces of (a) pump of laser A, (b) intensity of laser A, (c) intensity of laser B, (d) phase difference between lasers B and A divided by 2π, and (e) output ratio parameter defined in the text, for operating conditions given in the text.

equilibrium. Notably, the spikes fired by the system are of high-speed nature, with typical temporal durations of order 100 ps and sub-nanosecond inter-spike timing intervals. This behaviour is very similar to that found for optically-injected lasers in the analysis by Hurtado and Javaloyes [46]. In the fourth column (Fig. 1(j–l)), spiking inhibition is demonstrated where VCSEL A is operated at a slightly lower pumping rate ($Q_A = 33.32$) and all other parameters are identical to those given above. This situation yields continuous high-speed spiking behaviour and corresponds to $q = 0.8575$ with the SN boundary at 2.45 GHz. The spikes are subsequently controllably inhibited by the application of a positive pulse to the pump current of VCSEL A (Fig. 1(j)) of amplitude +5 and duration 5 ns. Again, this behaviour is similar to that previously demonstrated in optically-injected VCSELs [14]. In the activation case, the depth of the negative current pulse in VCSEL A determines the number of spikes and their frequency and the system finds stable equilibrium when (7) is satisfied (note the similarity to the stability condition derived in [46]). In the case of the optically-injected laser [46], the determining parameter is the amplitude Y_A of the optical injection. The example of Fig. 1 and the analogy with spiking in optically-injected lasers shows the sensitivity of the coupled-laser system to small variations of parameter values in the vicinity of the SN bifurcation.

B. Rebound Spiking

Under certain operating conditions, a short negative pump pulse applied to VCSEL A can also trigger a spike from VCSEL B immediately after the pulse, i.e. a 'rebound spike' [47]. An example of this is shown in Fig. 2 where the parameter values are $|\eta| = 3.9$ ns^{-1}, $\Delta\Omega/2\pi = 3.4$ GHz, $q = 0.8$, $Q_A = 23.32$ and others as above, with a 2 ns negative pulse of depth 4.5. Fig. 2(a)–(e) show, respectively, time traces of the normalised pump Q_A, intensities $I_j = Y_j^2$ ($j = A, B$), phase $\phi/2\pi$ and ψ defined [44] by:

$$\frac{Y_B}{Y_A} = \tan\left(\frac{\psi}{2} + \frac{\pi}{4}\right) \tag{9}$$

Further insight into the spiking behaviour can be gained from study of phase portraits, a 3D example of which is shown in Fig. 3(a) with projection on the 2D plane of (m, ψ) in Fig. 3(b), where $m = M_A - M_B$. In order to analyse the features of the phase portrait, we note here the following results for steady-state solutions of the 3-variable reduction of the coupled mode equations with $\theta = -\pi/2$:

$$\psi_s \simeq \arcsin(-q) \tag{10}$$

$$m_s \simeq \frac{4|\eta|\tau_p q}{\sqrt{1 - q^2}} \cos(\phi_s) \tag{11}$$

$$\phi_s \simeq \pm \arccos\left(\frac{\Delta\Omega}{2|\eta|}\sqrt{\frac{1 - q^2}{1 + a_H^2 q^2}}\right) - \arctan\left(\frac{1}{a_H q}\right) \tag{12}$$

where the subscript s denotes the steady-state value. In (12), the plus and minus signs correspond to the tilted in-phase and tilted out-of-phase solutions, following the nomenclature introduced first by Gao et al. [42].

The sequence of events to produce this 'rebound spike' is that when the pump pulse ends, the system first goes to a quasi-steady-state with the tilted out-of-phase solution (and there is ringing in VCSEL A). It then returns to a stable steady-state tilted in-phase solution (and, as it does so, a spike is emitted from VCSEL B with some very damped ringing). Arrows have been added to the trajectories in Fig. 3(b) in order to show the temporal sequence. For the steady-state situation before and after the pump pulse, $q = 0.8$ and hence (10)–(12) for the tilted in-phase solution give $\psi_s = -0.93$, $m_s = 0.032$ and $\phi_s/2\pi = -0.007$ (modulus 2π). These values are given in the co-ordinates of the points indicated on Fig. 3(b) and are in reasonable agreement with the points predicted by the numerical solution. For the steady-state situation during the pulse, $q = 0.756$ and hence (10)–(12) for the tilted in-phase solution give $\psi_s = -0.86$, $m_s = 0.025$ and $\phi_s/2\pi = -0.07$. When the pulse ends, the system goes to the quasi-steady-state tilted out-of-phase solution $\psi_s = -0.93$, $m_s = 0.015$ and $\phi_s/2\pi = -0.17$ before returning to the stable tilted in-phase solution with the usual phase shift of 2π. Again, comparison of these values for the co-ordinates of the points indicated on Fig. 3(b) are in agreement with the numerical results. These comparisons demonstrate the validity of the 3-variable reduction of the coupled mode equations and give valuable assistance to interpretation of the detailed features of the phase portraits.

C. Values of Coupling Phase Other Than $\pi/2$

In the discussion thus far, we have focused on the assumption of coupling phase $\theta = \pm\pi/2$ by analogy with the situation in optically-injected lasers, as discussed in Section III-A. However, it is worth noting that spiking behaviour in laterally-coupled VCSELs is also found in cases where this assumption is not made. For example, consider the complex coupling discussed in [31], Table I, line 1, where the lasers are assumed to have positive index guiding with some gain guiding, e.g. as in the case of oxide-aperture VCSELs, and a simple slab waveguide

(0.025,-0.86) stability during pulse

spike

(0.015,-0.93) quasi-steady-state (tilted out-of-phase)

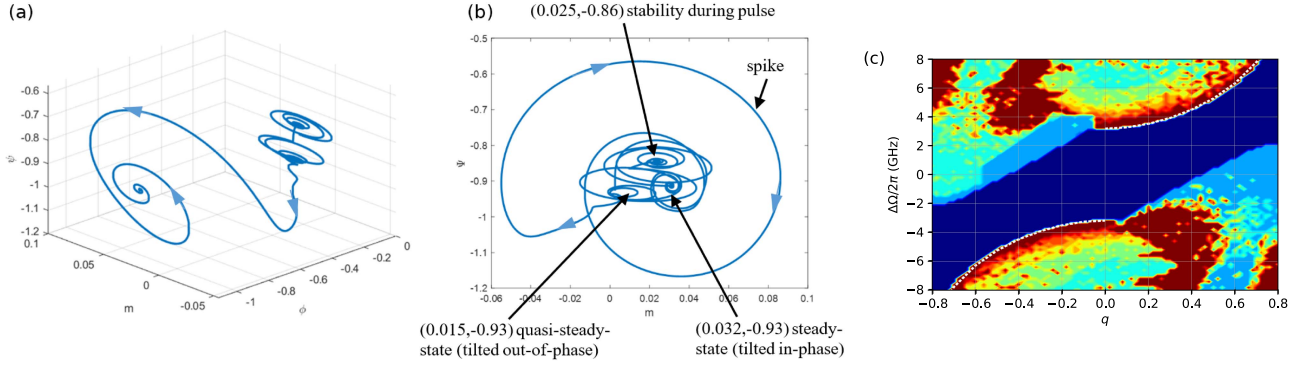(0.032,-0.93) steady-state (tilted in-phase)

Fig. 3. Phase portraits in (a) $(\phi/2\pi, m, \psi)$ space and (b) (m, ψ) space, corresponding to the results of Fig. 2. (c) Stability map for $|\eta| = 10.2$ ns^{-1} and $\theta = -1.559$ with $\tau_N = 1$ ns, $\tau_p = 1.53$ ps, and $\alpha_H = 2$. The white dotted lines indicate the SN boundaries as predicted from (5). Dark blue indicates stability, lighter blue, green and yellow correspond to periodicity, whilst orange and red denote more complicated dynamics and chaos.

TABLE I
PARAMETER VALUES USED IN THIS PAPER

Fig.	$|\eta|$ (ns^{-1})	θ	Q_A	Q_B	$\Delta\Omega/2\pi$ (GHz)	Comments
1(a)-(i)	2	$-\pi/2$	38.32	3.48	2.6	Spiking activation
1(j)-(l)	2	$-\pi/2$	33.32	3.48	2.6	Spiking inhibition
2, 3(a)-(b)	3.9	$-\pi/2$	23.32	3.48	3.4	Rebound spiking with phase portraits
3(c)	10.2	-1.559	Varied, keeping $Q_A + Q_B = 26$	Varied from -7.5 to 7.5		Stability map, comparison of SN boundary with Eq. 5
4	10.2	-1.559	(13,13), (17.8,8.2), (20.2,5.8), (22.6,3.4)		3.2, 4.5, 6.2, 9.7	Spiking behaviour close to SN boundary
5 - 8	3.3	$\pi/2$	5.85	2	2	Spike processing functions

structure is used to calculate the complex coupling rate. For the parameter values $d/a = 1$ considered in [31], $|\eta| = 10.2$ ns^{-1} and $\theta = -1.559$. A stability map in the plane of detuning versus q is shown in Fig. 3(c) for this system. This is obtained by first computing a numerical (Runge-Kutta) time series solution of the rate equations (1)–(4) for each point on the map. From these time series, one-parameter bifurcation diagrams are constructed at each value of q and detuning, and these are then used to construct the stability map. Examples of one-parameter bifurcation diagrams are given in Figs. 5 and 9 of [31] and details of how these are used to construct stability maps are given in [48]. Areas of stability are indicated in dark blue, regions of periodicity are denoted by lighter blue, green and yellow colours, whilst areas of more complicated dynamics and chaos are in orange and red. In contrast, the white dotted lines indicate the predicted SN boundaries that are readily identified from (5) demonstrating good agreement with the stability boundaries obtained more rigorously in the map.

Equation (5) predicts the stability boundary to be at 3.17 GHz for $q = 0$, 4.48 GHz for $q = 0.4$, 6.30 GHz for $q = 0.6$, and 10.2 GHz for $q = 0.8$. To investigate the possibility of spiking behaviour near these values, the other parameter values are as before, i.e. $\tau_N = 1$ ns, $\tau_p = 1.53$ ps, $\alpha_H = 2$, and the total pumping ($Q_A + Q_B$) is fixed at 26 (which corresponds to twice threshold in both lasers in the model of [31]). Fig. 4 shows the computed time series with spiking occurring at detunings of 3.2 GHz for $q = 0$, 4.45 GHz for $q = 0.4$, 6.15 GHz for $q = 0.6$, and 9.7 GHz for $q = 0.8$. This example indicates the abundance of operating conditions where spiking behaviour can be predicted to occur. Other examples with different sets of
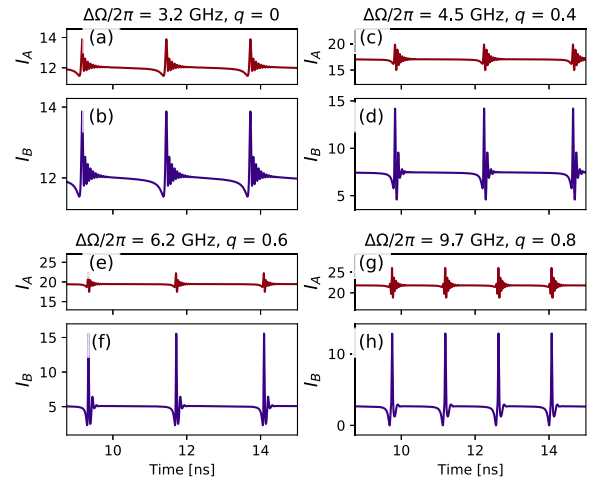

Fig. 4. Spiking behaviour computed for the detunings and pumping ratios indicated for system of Fig. 3(c).

complex coupling rates are also easily demonstrated by working close to the stability boundary given by (5), assuming weak coupling ($|\eta|\tau_p \ll 1$). As an extreme case, it is also possible to find spiking behaviour in the case of real coupling rates.

In order to provide clarity on the range of parameter values used in our numerical work to demonstrate various attributes of the spiking phenomena, Table I lists the varying parameter values corresponding to each Figure with comments on each case.

While the range of used $Q_{A,B}$ values is large, it does not mean that the VCSELs are being simulated over an unrealistic range thanks to the following relation between normalised pumps $Q_{A,B}$ and real pump P [31]:

$$Q = C_Q \left(\frac{P}{P_{th}} - 1\right) + \frac{P}{P_{th}} \quad (13)$$

where C_Q is a parameter related to the threshold gain and other VCSEL parameters. Taking $C_Q = 11$ (value in range of previous slab waveguide model [31]), a high value of Q such as $Q = 38.32$
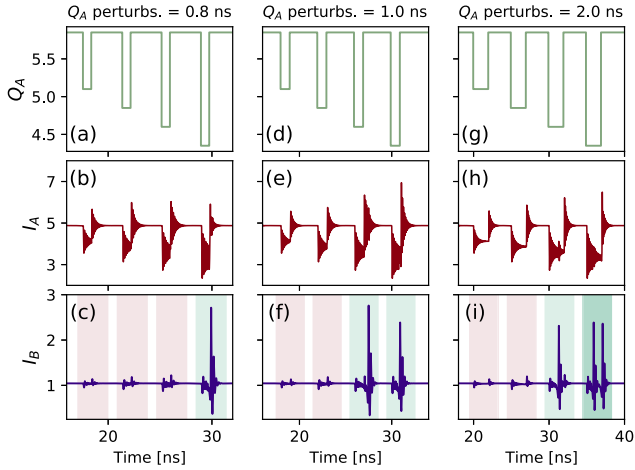
Fig. 5. Demonstration of spiking threshold on activation pulses. The traces shown include normalised pump for VCSEL A (upper row), output intensities of VCSEL A (middle row) and output intensity of VCSEL B (bottom row). $Q_A = 5.85$, $Q_B = 2$, $|\eta_{AB}| = |\eta_{BA}| \equiv |\eta| = 3.3$ ns^{-1}, $\theta = \pi/2$, $\Delta\Omega = 4\pi$ rad/ns. Responses are shown for: (a–c) perturbations of 800 ps; (d–f) perturbations of 1 ns; (g–i) perturbations of 2 ns. The depth of perturbations (dips) in Q_A is gradually increased in -0.25 amplitude increments in all cases, resulting in a single spiking event for $Q_{A-dip} = -1.5$ for 800 ps (shown in (c)) and for -1.25 (shown in (f),(i)). A spike is not elicited by the third perturbation in (c) since there is insufficient energy as a result of the short length of the pulse. Other parameters remain same as for previous figures.

corresponds to $\frac{P}{P_{th}} = 4.1$, well within the realistic ranges used for VCSELs.

IV. PHOTONIC SPIKE PROCESSING FUNCTIONALITIES

The results provided above suggest that many of the functionalities and potential applications of spiking lasers that have been proposed and demonstrated using optical injection and polarisation dynamics in discrete standard VCSELs [17], [18], [19], [24], [25], [49] could be achieved using photonic spiking neurons based upon laterally-coupled pairs of VCSELs. In this section, we will utilize some of the fundamental neuro-inspired dynamical behaviours observed in the laterally-coupled two-VCSEL numerical model that are key for realization of a neuromorphic system. These include: a) a well-defined excitable threshold with optional adjustability, which we utilize for high-speed photonic digital-to-spiking conversion with precise spike timing, and b) rate-modulated spike firing, allowing for encoding of input stimuli into continuous fast optical spike trains, which we utilize for encoding of digital image pixel values.

A. Spike Activation Threshold

Firstly, we demonstrate the existence of a well defined activation threshold in perturbation strength for spiking in the laterally-coupled VCSELs, which can be observed for negative input pulses (stimuli) of increasing depth for three different temporal lengths, applied to the normalized pump rate (Q_A) within a laser pair that is biased for stable operation. Fig. 5(a) shows the modulation pattern of 800 ps pulses applied to Q_A, whilst
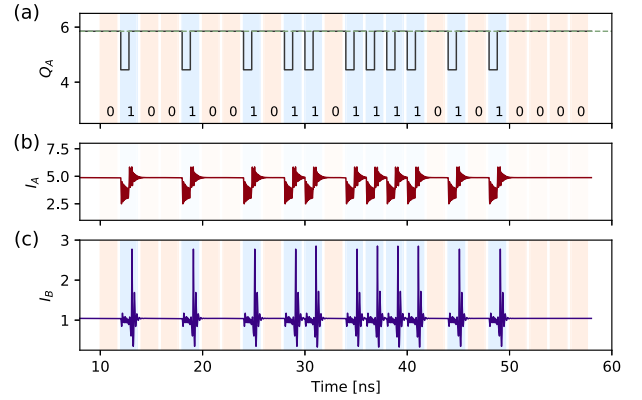

Fig. 6. Demonstration of direct digital-to-spike encoding functionality. The encoded word is "IoP" encoded in ASCII binary representation. (a) Normalised pump for laser A; (b) and (c) output intensities for VCSEL A (b) and VCSEL B (c). $Q_A = 5.85$, $Q_B = 2$, $|\eta_{AB}| = |\eta_{BA}| \equiv |\eta| = 3.3$ ns^{-1}, $\theta = \pi/2$, $\Delta\Omega = 4\pi$ rad/ns. The 0.8ns-long perturbations (dips) have an amplitude -1.5 (local $Q_A = 4.35$ during the perturbation).

Fig. 5(b–c) show the optical outputs of VCSELs A and B respectively. The same mechanism is then shown for 1 ns perturbations in Fig. 5(d–f) and for 2 ns perturbations in Fig. 5(g–i). VCSEL A responds to the applied Q_A pulse with a dip in intensity, as expected. However, VCSEL B does not respond significantly until a threshold is reached, after which a fast (sub-nanosecond) spike in output is activated (Fig. 5(c)), exhibiting a clear all-or-nothing spiking response. When eliciting spikes with perturbations, the temporal length of a perturbation matters, and very short pulses might have insufficient effect on the system despite having amplitude above threshold. This is an expected behaviour, as the system does not have infinite bandwidth and will therefore not recognize pulses of completely arbitrary temporal lengths (even if they adhere to the super-threshold amplitude condition). This is shown in Fig. 5(d–f), where the 3 rd perturbation now also has a sufficient energy (power × pulse length) to elicit a spike thanks to being 200 ps longer. Further extension of pulse length in Fig. 5(g) does not yield spiking from lower amplitude perturbations. The double spike observed in Fig. 5(i) is consistent with phenomena observed in Fig. 1 for long pulses. The thresholding behaviour in Fig. 5 can be understood in terms of the relation between the detuning $\Delta\Omega$ and the angular frequency of the saddle-node bifurcation as defined by the approximate expression in (8). For the detuning $\Delta\Omega = 4\pi$ rad/ns, equality in (8) is found for $Q_A = 4.84$. It follows that, within the limits of the approximation leading to (8), spiking is not expected for the first two pulses since the system is then in a region of stability.

B. Digital-to-Spike Conversion Task

We utilize the capability of spiking thresholding of the laterally-coupled VCSEL neuronal model to perform a conversion of digitally represented data into a sequence of spikes (a spike train) at fast data rates. In Fig. 6, we encode the word "IoP", acronym of Strathclyde's Institute of Photonics, represented in ASCII binary code utilizing an RZ encoding
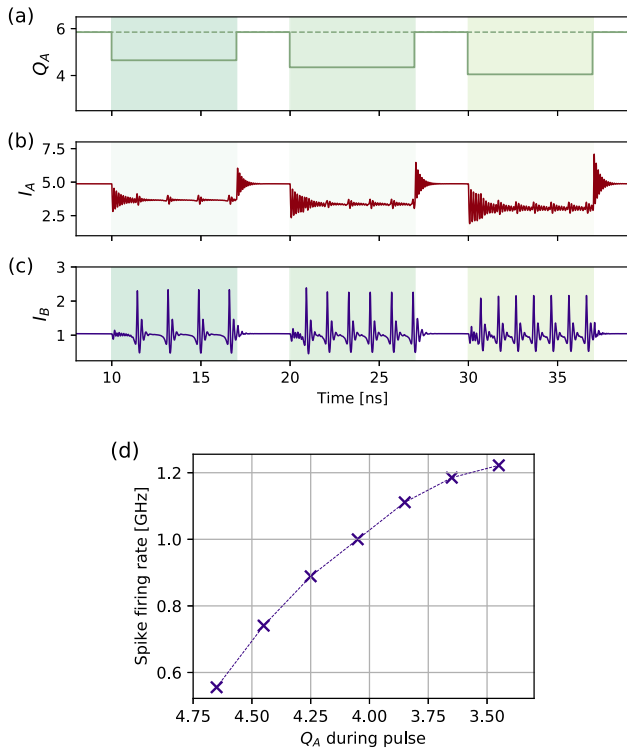
Fig. 7. Demonstration of different spiking frequencies produced by modulations with varying amplitude. (a) Pump intensity of VCSEL A; (b) Output intensities for VCSEL A and (c) VCSEL B. (d) Scatter plot of local spiking frequency as a function of input perturbation amplitude. The parameter values used are the same as for Figs. 5 and 6.
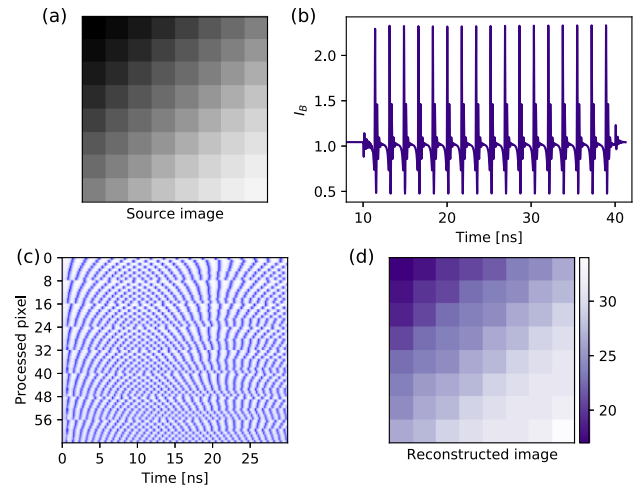

Fig. 8. Rate-coded representation of an 8x8 greyscale diagonal graded image. (a) Source image. (b) Demonstration of a spiking time-trace containing information for a single pixel. Only the 30 ns interval with active spiking is depicted. (c) Temporal map merging in a single plot spiking time-traces for all processed source pixels. Only the 30 ns-pixel intervals with active spiking are depicted. (d) Direct reconstruction of the source image from the spiking rates obtained for each pixel. .

scheme at a rate of 2 ns/bit and 40% duty cycle. As can be seen in Fig. 6(c), the system is capable of reliable generation of optical spikes by means of input signal power thresholding, allowing for (among others) digital-to-spike conversion functionality.

C. Spike Rate-Coding for Digital Images

The ability to produce continuous (tonic) spiking regimes is also highly desirable for spike-based information representation utilizing the temporal domain. In particular, rate-coding, where the information about incoming stimuli is encoded into the spiking firing frequency of continuous spike trains [17], constitutes one of the approaches utilized by certain classes of biological neurons for information representation. Previous results (Fig. 1) confirm that the laterally-coupled VCSEL-neuronal system is capable of producing spikes at varying rates (Fig. 7). We show that the optical output of VCSEL B in a laterally-coupled VCSEL system produces continuous spike trains, when subject to time-varying modulation of normalized pump Q_A. We utilize square-shaped pulses to directly encode a constant local spiking frequency, but want to emphasize that this is an analogue-to-spiking conversion method that also supports continuous (analog) modulation signals and directly encodes those into the rate-coded spike-based representation. We can see in Fig. 7(c), that for pump modulation pulses with higher pulse amplitudes (deeper dips), the spike firing frequency increases in

a monotonic fashion, and this is quantified in Fig. 7(d) as spike firing rate versus Q_A during the pulse.

Fig. 8 demonstrates how the ability of the laterally-coupled VCSEL neuronal model to produce modulation-dependent spiking firing rates can be utilized to perform direct encoding of information from digital images into high-speed rate-coded spiking representations [19]. In the proof-of-concept demonstration of Fig. 8, we used an 8×8 pixel greyscale graded pattern as the source image. All the pixels in the source 8 x 8 greyscale image (Fig. 8(a)) are serialised into a single input stream using time-domain multiplexing (TDM) to enable their processing with a single pair of laterally-coupled VCSELs. The intensity of each pixel is encoded with amplitude values between 0 and 1. The sequence of (0,1)-bounded pixel values is used as a Q_A (normalized pump) modulation source, where each pixel is time multiplexed and turned into pulses of length $t_{ON} = 30$ ns, with $t_{OFF} = 5$ ns spacing. The n-th pixel value was directly encoded into the pulse (dip) amplitude following the formula $\Delta Q_{An} = -1.2 - p_n$ where ΔQ_{An} is the dip amplitude, and p_n is the n-th pixel greyscale intensity value bounded between (0,1). Using this approach, the number of spikes generated by VCSEL B in the laterally-coupled VCSEL-neuron pair directly encodes the intensity of each pixel in the source greyscale image. For each pixel, the spikes fired were counted and used to create a direct image reconstruction (Fig. 8(d)) of the originally encoded greyscale source image. Directly comparing Fig. 8(a) and Fig. 8(d) reveals very good agreement between the source and direct spike-count-based reconstruction images; hence confirming the system's ability to encode the image pixels information in the spike firing rate. We also note that there were instances of more than 30 spikes counted in the 30 ns interval, as can be seen in the colour-map bar in Fig. 8(d), representing encoding at higher than GHz spiking rates.

D. Comparison of Laterally-Coupled VCSELs With Optically-Injected VCSELs for Neuromorphic Tasks

It is appropriate here to consider the relative merits of laterally-coupled VCSEL pairs compared with optically-injected VCSELs for use as spiking neurons. We have shown already that these two systems can be used in similar applications and offer similar performance. As a source of optical spiking, one major advantage of the coupled VCSEL system is the elimination of the need for a tightly controlled (in terms of polarisation, wavelength, detuning and power) external master laser. In contrast, with these key parameters of polarisation, coupling and detuning being built in at fabrication stage, and with bias being a control parameter, laterally coupled VCSELs offer a simpler overall prospect with additional robustness. In photonic crystal VCSELs, elliptical air holes in the top mirror have been experimentally demonstrated to control polarisation [50] and holes of different sizes on opposite sides of the array can realize asymmetric coupling [33]. This asymmetry controls the detuning between the cavities. Additional (unwanted) detuning caused by fabrication imperfections can be corrected by pump currents control [33].

When considering more complex computational systems requiring multiple coupled elements, scaling up the number of externally injected spiking VCSELs presents significant challenges both in terms of their physical complexity and their control. Here we believe laterally coupled VCSELs offer multiple significant advantages. Nevertheless, a challenge peculiar to a closely-spaced laterally-coupled pair of VCSELs is the spatial separation of optical inputs and outputs. While this might be achieved using spatially selective optics, e.g. lenses or lens-ended fibres, this is not a scalable approach for larger, more complex arrays. However, as the circuit size grows, and with more on-chip processing, both the number and density of optical i/p and o/p connections can be reduced, thus easing these requirements. Moreover, by varying the key design parameters, it is possible to build in a degree of spatial heterogeneity to provide areas of different functionality (for example, an external coupling region) while preserving the coupling. Such approach could be used to realize an extended optical lattice of devices, providing means of more extensive interconnectivity since the overall modes of the lattice can be influenced by individual elements. Alternatively, approaches such as 3D printed multimode splitters [51] may offer an interlinking solution for building neuromorphic photonic circuits capable of diverse range of information processing tasks.

V. Conclusion

Coupled-mode rate equations have been used to demonstrate the existence of ultrafast spiking behaviour in weakly-coupled pairs of VCSELs when operated at frequency detunings in the vicinity of the SN stability boundary. Upon appropriate choice of continuous wave pumping values, the system of this work shows its ability to generate or inhibit controllable spiking patterns in one VCSEL by injecting pulses of negative or positive polarity into the pump of the other VCSEL. In addition to excitation of phasic and tonic spiking regimes, rebound spiking dynamics after the end of an input pulse are also demonstrated. It has been shown that this rebound spiking response is associated with a switch between tilted out-of-phase and in-phase states of the system of laterally-coupled VCSELs. Preliminary results for the case of purely imaginary coupling coefficients have been extended to the case of arbitrary complex coupling, provided always that operation is limited to the region of the SN bifurcation. This opens the way to experimental tests of these predictions, since there already exist several practical demonstrations of various forms of dynamical behaviours in arrays of coupled VCSELs (see, for example, [32], [33]). Experimental methods to measure the real and imaginary parts of the complex coupling coefficient in such arrays have been reported [43], thus enabling relatively accurate device modelling to be performed in order to identify operating conditions for spiking, following the approach suggested here. Finally, we also report numerically on the potential of the investigated spiking regimes in laterally-coupled VCSEL systems for use in different practical photonic spike processing functionalities. These are based on the precise spike timing and spiking rate-coding capabilities demonstrated in the proposed laterally-coupled VCSEL photonic neuronal model, and include digital-to-spike format conversion and spike rate-coding of digital image information.

References

[1] P. R. Prucnal, B. J. Shastri, T. Ferreira de Lima, M. A. Nahmias, and A. N. Tait, "Recent progress in semiconductor excitable lasers for photonic spike processing," *Adv. Opt. Photon.*, vol. 8, no. 2, 2016, Art. no. 228. [Online]. Available: https://www.osapublishing.org/abstract.cfm?URI=aop-8-2-228

[2] B. J. Shastri et al., "Photonics for artificial intelligence and neuromorphic computing," *Nature Photon.*, vol. 15, no. 2, pp. 102–114, 2021. [Online]. Available: http://www.nature.com/articles/s41566-020-00754-y

[3] G. Sarantoglou, M. Skontranis, and C. Mesaritakis, "All optical integrate and fire neuromorphic node based on single section quantum dot laser," *IEEE J. Sel. Topics Quantum Electron.*, vol. 26, no. 5, pp. 1–10, Sep./Oct. 2020. [Online]. Available: https://ieeexplore.ieee.org/document/8864022/

[4] H.-T. Peng, M. A. Nahmias, T. F. de Lima, A. N. Tait, and B. J. Shastri, "Neuromorphic photonic integrated circuits," *IEEE J. Sel. Topics Quantum Electron.*, vol. 24, no. 6, pp. 1–15, Nov./Dec. 2018. [Online]. Available: https://ieeexplore.ieee.org/document/8364605/

[5] H.-T. Peng et al., "Temporal information processing with an integrated laser neuron," *IEEE J. Sel. Topics Quantum Electron.*, vol. 26, no. 1, pp. 1–9, Jan./Feb. 2020. [Online]. Available: https://ieeexplore.ieee.org/document/8760358/

[6] F. Selmi et al., "Spike latency and response properties of an excitable micropillar laser," *Phys. Rev. E*, vol. 94, no. 4, 2016, Art. no. 042219. [Online]. Available: https://link.aps.org/doi/10.1103/PhysRevE.94.042219

[7] W. Coomans et al., "Solitary and coupled semiconductor ring lasers as optical spiking neurons," *Phys. Rev. E*, vol. 84, no. 3, 2011, Art. no. 036209. [Online]. Available: https://link.aps.org/doi/10.1103/PhysRevE.84.036209

[8] M. Brunstein et al.,, "Excitability and self-pulsing in a photonic crystal nanocavity," *Phys. Rev. A*, vol. 85, no. 3, 2012, Art. no. 031803. [Online]. Available: https://link.aps.org/doi/10.1103/PhysRevA.85.031803

[9] F. Laporte, A. Katumba, J. Dambre, and P. Bienstman, "Numerical demonstration of neuromorphic computing with photonic crystal cavities," *Opt. Exp.*, vol. 26, no. 7, 2018, Art. no. 7955. [Online]. Available: https://www.osapublishing.org/abstract.cfm?URI=oe-26-7-7955

[10] B. J. Shastri et al.,, "Spike processing with a graphene excitable laser," *Sci. Rep.*, vol. 6, no. 1, 2016, Art. no. 19126. [Online]. Available: http://www.nature.com/articles/srep19126

[11] B. Romeira, R. Avó, J. M. L. Figueiredo, S. Barland, and J. Javaloyes, "Regenerative memory in time-delayed neuromorphic photonic resonators," *Sci. Rep.*, vol. 6, no. 1, 2016, Art. no. 19510. [Online]. Available: http://www.nature.com/articles/srep19510

[12] M. Hejda et al., "Resonant tunneling diode nano-optoelectronic excitable nodes for neuromorphic spike-based information processing," *Phys. Rev. Appl.*, vol. 17, no. 2, 2022, Art. no. 024072.

[13] A. Skalli et al., "Photonic neuromorphic computing using vertical cavity semiconductor lasers," *Opt. Mater. Exp.*, vol. 12, no. 6, pp. 2395–2414, 2022, [Online]. Available: https://opg.optica.org/abstract.cfm?URI=ome-12-6-2395

[14] J. Robertson, T. Deng, J. Javaloyes, and A. Hurtado, "Controlled inhibition of spiking dynamics in VCSELs for neuromorphic photonics: Theory and experiments," *Opt. Lett.*, vol. 42, no. 8, 2017, Art. no. 1560.

[15] Y. Lu, W. Zhang, B. Fu, and Z. He, "Frequency-switched photonic spiking neurons," *Opt. Exp.*, vol. 30, no. 12, 2022, Art. no. 21599. [Online]. Available: https://opg.optica.org/abstract.cfm?URI=oe-30-12-21599

[16] J. Robertson, E. Wade, and A. Hurtado, "Electrically controlled neuron-like spiking regimes in vertical-cavity surface-emitting lasers at ultra-fast rates," *IEEE J. Sel. Topics Quantum Electron.*, vol. 25, no. 6, pp. 1–7, Nov./Dec. 2019. [Online]. Available: https://ieeexplore.ieee.org/document/8653910/

[17] M. Hejda, J. Robertson, J. Bueno, and A. Hurtado, "Spike-based information encoding in vertical cavity surface emitting lasers for neuromorphic photonic systems," *J. Physics: Photon.*, vol. 2, no. 4, 2020, Art. no. 044001. [Online]. Available: https://iopscience.iop.org/article/10.1088/2515-7647/aba670

[18] J. Robertson et al., "Ultrafast neuromorphic photonic image processing with a VCSEL neuron," *Sci. Rep.*, vol. 12, no. 1, 2022, Art. no. 4874. [Online]. Available: https://www.nature.com/articles/s41598-022-08703-1

[19] M. Hejda, J. Robertson, J. Bueno, J. A. Alanis, and A. Hurtado, "Neuromorphic encoding of image pixel data into rate-coded optical spike trains with a photonic VCSEL-neuron," *APL Photon.*, vol. 6, no. 6, 2021, Art. no. 060802. [Online]. Available: https://aip.scitation.org/doi/10.1063/5.0048674

[20] T. Deng, J. Robertson, and A. Hurtado, "Controlled propagation of spiking dynamics in vertical-cavity surface-emitting lasers: Towards neuromorphic photonic networks," *IEEE J. Sel. Topics Quantum Electron.*, vol. 23, no. 6, pp. 1–8, Nov./Dec. 2017. [Online]. Available: https://ieeexplore.ieee.org/document/7885010/

[21] M. A. Nahmias, B. J. Shastri, A. N. Tait, and P. R. Prucnal, "A leaky integrate-and-fire laser neuron for ultrafast cognitive computing," *IEEE J. Sel. Topics Quantum Electron.*, vol. 19, no. 5, pp. 1–12, Sep./Oct. 2013. [Online]. Available: https://ieeexplore.ieee.org/document/6497478/

[22] Y. Han, S. Xiang, Z. Song, A. Wen, and Y. Hao, "Spiking dynamics and synchronization properties of optical neurons based on VCSEL-SAs," *Nonlinear Dyn.*, vol. 105, no. 3, pp. 2665–2675, 2021. [Online]. Available: https://link.springer.com/10.1007/s11071-021-06699-3

[23] S. Xiang et al., "Computing primitive of fully VCSEL-based all-optical spiking neural network for supervised learning and pattern classification," *IEEE Trans. Neural Netw. Learn. Syst.*, vol. 32, no. 6, pp. 2494–2505, Jun. 2021. [Online]. Available: https://ieeexplore.ieee.org/document/9142407/

[24] Y. Zhang, S. Xiang, X. Guo, A. Wen, and Y. Hao, "The winner-take-all mechanism for all-optical systems of pattern recognition and max-pooling operation," *J. Lightw. Technol.*, vol. 38, no. 15, pp. 5071–5077, Sep. 2020. [Online]. Available: https://ieeexplore.ieee.org/document/9110773/

[25] Z. Song, S. Xiang, Z. Ren, G. Han, and Y. Hao, "Spike sequence learning in a photonic spiking neural network consisting of VCSELs-SA with supervised training," *IEEE J. Sel. Topics Quantum Electron.*, vol. 26, no. 5, pp. 1–9, Sep./Oct. 2020. [Online]. Available: https://ieeexplore.ieee.org/document/9018042/

[26] S. Gao et al.,, "Motion detection and direction recognition in a photonic spiking neural network consisting of VCSELs-SA," *Opt. Exp.*, vol. 30, no. 18, 2022, Art. no. 31701. [Online]. Available: https://opg.optica.org/abstract.cfm?URI=oe-30-18-31701

[27] M. Ahmed, A. Bakry, M. S. Alghamdi, H. Dalir, and F. Koyama, "Enhancing the modulation bandwidth of VCSELs to the millimeter-waveband using strong transverse slow-light feedback," *Opt. Exp.*, vol. 23, no. 12, pp. 15365–15371, 2015. [Online]. Available: https://opg.optica.org/oe/abstract.cfm?uri=oe-23-12-15365

[28] S. Hu et al.,, "1060-nm single-mode transverse coupled cavity VCSEL with intra-cavity surface relief for 58-gbps modulation and 5-km single-mode fiber transmission," *Appl. Phys. Lett.*, vol. 120, no. 26, 2022, Art. no. 261110. [Online]. Available: https://aip.scitation.org/doi/10.1063/5.0094252

[29] C. Hao et al., "Dynamics of high-contrast grating vertical-cavity surface-emitting laser with lateral optical feedback by a heterostructure interface," *Opt. Exp.*, vol. 30, no. 12, pp. 22074–22087, 2022. [Online]. Available: https://opg.optica.org/oe/abstract.cfm?uri=oe-30-12-22074

[30] E. Heidari, H. Dalir, M. Ahmed, V. J. Sorger, and R. T. Chen, "Hexagonal transverse-coupled-cavity VCSEL redefining the high-speed lasers," *Nanophotonics*, vol. 9, no. 16, pp. 4743–4748, 2020. [Online]. Available: https://www.degruyter.com/document/doi/10.1515/nanoph-2020-0437/html

[31] M. J. Adams, N. Li, B. R. Cemlyn, H. Susanto, and I. D. Henning, "Effects of detuning, gain-guiding, and index antiguiding on the dynamics of two laterally coupled semiconductor lasers," *Phys. Rev. A*, vol. 95, no. 5, 2017, Art. no. 053869. [Online]. Available: http://link.aps.org/doi/10.1103/PhysRevA.95.053869

[32] G. Pan et al., "Analysis of optical coupling behavior in two-dimensional implant-defined coherently coupled vertical-cavity surface-emitting laser arrays," *Photon. Res.*, vol. 6, no. 11, 2018, Art. no. 1048. [Online]. Available: https://opg.optica.org/abstract.cfm?URI=prj-6-11-1048

[33] H. Dave, Z. Gao, S. T. M. Fryslie, B. J. Thompson, and K. D. Choquette, "Static and dynamic properties of coherently-coupled photonic-crystal vertical-cavity surface-emitting laser arrays," *IEEE J. Sel. Topics Quantum Electron.*, vol. 25, no. 6, pp. 1–8, Nov./Dec. 2019. [Online]. Available: https://ieeexplore.ieee.org/document/8717703/

[34] X. Guo, J. Xiang, Y. Zhang, and Y. Su, "Integrated neuromorphic photonics: Synapses, neurons, and neural networks," *Adv. Photon. Res.*, vol. 2, no. 6, 2021, Art. no. 2000212. [Online]. Available: https://onlinelibrary.wiley.com/doi/10.1002/adpr.202000212

[35] R. Al-Seyab, I. D. Henning, M. J. Adams, and A. Hurtado, "Controlled single- and multiple-pulse excitability in VCSELs for novel spiking photonic neurons," in *Proc. IEEE Int. Semicond. Laser Conf.*, vol. 1, 2014, pp. 165–166. [Online]. Available: https://ieeexplore.ieee.org/document/6987502/

[36] S. Xiang et al., "Cascadable neuron-like spiking dynamics in coupled VCSELs subject to orthogonally polarized optical pulse injection," *IEEE J. Sel. Topics Quantum Electron.*, vol. 23, no. 6, pp. 1–7, Nov./Dec. 2017. [Online]. Available: https://ieeexplore.ieee.org/document/7872477/

[37] S. Xiang, A. Wen, and W. Pan, "Emulation of spiking response and spiking frequency property in VCSEL-based photonic neuron," *IEEE Photon. J.*, vol. 8, no. 5, pp. 1–9, Oct. 2016. [Online]. Available: https://ieeexplore.ieee.org/document/7577798/

[38] S. Xiang, Y. Zhang, X. Guo, A. Wen, and Y. Hao, "Photonic generation of neuron-like dynamics using VCSELs subject to double polarized optical injection," *J. Lightw. Technol.*, vol. 36, no. 19, pp. 4227–4234, Oct. 2018. [Online]. Available: https://ieeexplore.ieee.org/document/8322128/

[39] S. Wieczorek, B. Krauskopf, and D. Lenstra, "Multipulse excitability in a semiconductor laser with optical injection," *Phys. Rev. Lett.*, vol. 88, no. 6, 2002, Art. no. 063901. [Online]. Available: https://link.aps.org/doi/10.1103/PhysRevLett.88.063901

[40] H. Erzgräber, S. Wieczorek, and B. Krauskopf, "Dynamics of two laterally coupled semiconductor lasers: Strong- and weak-coupling theory," *Phys. Rev. E*, vol. 78, no. 6, 2008, Art. no. 066201. [Online]. Available: https://link.aps.org/doi/10.1103/PhysRevE.78.066201

[41] L. Gelens, S. Beri, G. Van der Sande, G. Verschaffelt, and J. Danckaert, "Multistable and excitable behavior in semiconductor ring lasers with broken z2-symmetry," in *Proc. Eur. Phys. J. D*, 2010, vol. 58, no. 2, pp. 197–207. [Online]. Available: http://link.springer.com/10.1140/epjd/e2010-00042-7

[42] Z. Gao, M. T. Johnson, and K. D. Choquette, "Rate equation analysis and non-hermiticity in coupled semiconductor laser arrays," *J. Appl. Phys.*, vol. 123, no. 17, 2018, Art. no. 173102. [Online]. Available: http://aip.scitation.org/doi/10.1063/1.5022044

[43] H. Dave, Z. Gao, and K. Choquette, "Complex coupling coefficient in laterally coupled microcavity laser diode arrays," *Appl. Phys. Lett.*, vol. 117, no. 4, 2020, Art. no. 041106. [Online]. Available: http://aip.scitation.org/doi/10.1063/5.0014468

[44] M. J. Adams, R. Al-Seyab, I. D. Henning, H. Susanto, and M. Vaughan, "Dynamics of evanescently-coupled laser pairs with unequal pumping: Analysis using a three-variable reduction of the coupled rate equations," *IEEE J. Sel. Topics Quantum Electron.*, vol. 28, no. 1, pp. 1–9, Jan./Feb. 2022. [Online]. Available: https://ieeexplore.ieee.org/document/9417616/

[45] F. Mogensen, H. Olesen, and G. Jacobsen, "Locking conditions and stability properties for a semiconductor laser with external light injection," *IEEE J. Quantum Electron.*, vol. 21, no. 7, pp. 784–793, Jul. 1985. [Online]. Available: https://ieeexplore.ieee.org/document/1072760/

[46] A. Hurtado and J. Javaloyes, "Controllable spiking patterns in long-wavelength vertical cavity surface emitting lasers for neuromorphic photonics systems," *Appl. Phys. Lett.*, vol. 107, no. 24, 2015, Art. no. 241103. [Online]. Available: http://aip.scitation.org/doi/10.1063/1.4937730

[47] A. Hurtado, K. Schires, I. D. Henning, and M. J. Adams, "Investigation of vertical cavity surface emitting laser dynamics for neuromorphic photonic systems," *Appl. Phys. Lett.*, vol. 100, no. 10, pp. 3–7, 2012.

[48] R. Al-Seyab, K. Schires, A. Hurtado, I. D. Henning, and M. J. Adams, "Dynamics of VCSELs subject to optical injection of arbitrary polarization," *IEEE J. Sel. Topics Quantum Electron.*, vol. 19, no. 4, Jul./Aug. 2013, Art. no. 1700512. [Online]. Available: https://ieeexplore.ieee.org/document/6417943/

[49] S. Xiang et al., "STDP-based unsupervised spike pattern learning in a photonic spiking neural network with VCSELs and VCSOAs," *IEEE J. Sel. Topics Quantum Electron.*, vol. 25, no. 6, pp. 1–9, Nov./Dec. 2019. [Online]. Available: https://ieeexplore.ieee.org/document/8693533/

[50] D.-S. Song, Y.-J. Lee, H.-W. Choi, and Y.-H. Lee, "Polarization-controlled, single-transverse-mode, photonic-crystal, vertical-cavity, surface-emitting lasers," *Appl. Phys. Lett.*, vol. 82, no. 19, pp. 3182–3184, 2003. [Online]. Available: https://aip.scitation.org/doi/10.1063/1.1574398

[51] J. Moughames et al., "3D printed multimode-splitters for photonic interconnects," *Opt. Mater. Exp.*, vol. 10, no. 11, 2020, Art. no. 2952. [Online]. Available: https://www.osapublishing.org/abstract.cfm?URI=ome-10-11-2952

Ian Henning received the Ph.D. degree from the University of Wales, Cardiff, U.K., in 1979. In 1980, he was with the Devices Division specializing in theory and measurements of semiconductor lasers, British Telecom Research Laboratories, Martlesham Heath, U.K. He joined the Department of Electrical Systems Engineering, Essex University, Colchester, U.K., in 2002, as a Professor. He has authored or co-authored numerous publications including research papers, books, and patents. His research interests mainly include the areas of optoelectronic devices, and electronic/photonic device integration.

Rihab Al-Seyab (Member, IEEE) received the Ph.D. degree in model predictive control from the University of Cranfield, Cranfield, U.K., in 2006, and the Ph.D. degree in dynamics of Spin-VCSELs (EPSRC Scholarship) from the University of Essex, Colchester, U.K., in 2013. In 2014, she was a Senior Research Fellow with the University of Essex, Senior Design Engineer with CIP Technologies, Huawei, Ipswich, U.K., during 2015–2016, and Principle Lecturer with the System Engineering Department, MTC/University of Portsmouth, Oman, during 2016–2019. She is currently a Senior Lecturer and Academic Course Leader of the M.Sc. Engineering Programs with the School of Computing and Engineering, University of Gloucestershire, Cheltenham, U.K. She is also a Visiting Fellow with Prof. Mike Adams and Prof. Ian Henning, University of Essex.

Matěj Hejda received the Ing. degree (MSc. equivalent) in Nanotechnology from the Technical University of Liberec, Czech Republic, in 2019. He is currently working toward the Ph.D. degree in physics with the Neuromorphic Photonics Group, Institute of Photonics, University of Strathclyde, Glasgow, U.K. His research mainly focuses on the investigation of spiking in photonic and optoelectronic devices towards applications in light-powered neuromorphic computing.

Antonio Hurtado received the Ph.D. degree from the Universidad Politécnica de Madrid, Madrid, Spain, in 2006. He is currently a Reader and Turing AI Fellow with the University of Strathclyde's Institute of Photonics, Glasgow, U.K. He has more than 15 years of international research experience in photonics in U.K., USA and Spain. In 2018, he become a Senior Lecturer and a Reader in 2021. In 2020 he was awarded a Turing AI Acceleration Fellowship by the U.K. Research and Innovation Office a five-year Research Programme on Photonics for Ultrafast AI. His research interests mainly include neuromorphic photonics, laser nonlinear dynamics, nanolaser systems, and hybrid nanofabrication. He was the recipient of the two Marie Curie Fellowships by the European Commission, Projects ISLAS (2009–2011) and NINFA (2011–2014), respectively, Chancellor's Fellowship by the University of Strathclyde, Glasgow, U.K., in 2014.

Martin Vaughan received the Ph.D. degree in electron transport and scattering in semiconductors from the University of Essex, Colchester, U.K., in 2007. From 2007 to 2009, he worked in different areas of semiconductor physics including THz devices. From 2009 to 2014, he worked in first principles band structure calculations and alloy scattering, Tyndall National Institute, Cork, Ireland. From 2017 to 2018, he worked in spin dynamics (Bristol, U.K.), and since 2019, he has worked in laser dynamics (Essex, U.K.). From 2014–2017, he also held a Physics Lectureship Position with University College Cork, Ireland and is currently in software development.

Mike Adams received the Ph.D. degree in laser theory from the University of Wales, Cardiff, U.K., in 1970. Since 1996, he has been a Professor with the University of Essex, Colchester, U.K. He is currently involved in optoelectronics Research and Development with 15 years of experience in industry, Plessey, BT, London, U.K., and 37 years in academia with the University of Cardiff, University of Southampton, Southampton, U.K., and University of Essex, Colchester, U.K. He has authored or coauthored widely in the optoelectronics field over many years, including a standard text on optical waveguide theory and two books on semiconductor lasers and optical fibres for use in telecommunications.